

## Evolution of domain structure in epitaxial ferroelectric $K_{0.5}Na_{0.5}NbO_3$ films grown by metal-organic vapor-phase epitaxy

Yankun Wang <sup>1,2</sup>, Saud Bin Anooz <sup>2</sup>, Gang Niu,<sup>1,3,\*</sup> Jinyan Zhao,<sup>1</sup> Martin Schmidbauer,<sup>2</sup> Lingyan Wang,<sup>1</sup> Wei Ren,<sup>1,3</sup> and Jutta Schwarzkopf<sup>2,†</sup>

<sup>1</sup>State Key Laboratory for Manufacturing Systems Engineering, Electronic Materials Research Laboratory, Key Laboratory of the Ministry of Education, School of Electronic Science and Engineering, Xi'an Jiaotong University, Xi'an 710049, China

<sup>2</sup>Leibniz-Institut für Kristallzüchtung (IKZ), Max-Born-Strasse 2, 12489 Berlin, Germany

<sup>3</sup>The International Joint Laboratory for Micro/Nano Manufacturing and Measurement Technology, Xi'an Jiaotong University, Xi'an 710049, China



(Received 31 October 2023; accepted 22 April 2024; published 13 May 2024)

Potassium sodium niobate lead-free piezoelectric thin films are of great potential for integrated functional devices. Metal-organic vapor-phase epitaxy enables high-quality wafer-scale fabrication of epitaxial piezoelectric thin films, whereas the film domain structure and evolution, which particularly originate from the strain and strongly impact the film properties, require further study. We report in this paper an in-depth study of the piezoelectric domain structure as well as the domain evolution induced by an external electric field in  $K_{0.5}Na_{0.5}NbO_3$  films. Epitaxially strained  $c_{pc}$  oriented  $K_{0.5}Na_{0.5}NbO_3$  films were grown on  $SrRuO_3/DyScO_3$  (110) substrates, and four different superdomain variants consisting of monoclinic  $90^\circ M_C$  stripe domains were verified and studied in detail. The domain switching behavior was examined by piezoresponse force microscopy (PFM), which suggests that both the in-plane and out-of-plane polarization can be reversed by an external out-of-plane positive electric field. However, application of a negative bias leads to the accumulation of surface charges concurrently accompanied by small morphology changes. We tentatively attribute this observation to the injection of vacancies in the film surface under negative voltage. Therefore, the out-of-plane polarization component cannot be switched, and in-plane orientation of the stripe domains is only reoriented at the edges of the litho-window, which could be attributed to either an inhomogeneous electric field below the PFM tip or trailing fields caused by the movement of the PFM tip across the surface. However, surface charges dissipate within 1 h. These results are beneficial for understanding the domain evolution mechanism and intentional tuning of ferroelectric thin-film properties.

DOI: [10.1103/PhysRevMaterials.8.054409](https://doi.org/10.1103/PhysRevMaterials.8.054409)

### I. INTRODUCTION

A typical phenomenon in ferroelectric materials is the formation of domains, which are essentially determined by the minimization of the elastic and electrostatic energies in the crystal [1,2]. The arrangement, orientation, and size of the domains all have a significant influence on the materials properties, including the piezoelectricity, the flexoelectricity, and the photoelectric performance [3,4]. Therefore, the functionality of corresponding technological devices must be ensured not only on a local atomic scale, but especially on a macroscopic scale. This is particularly relevant for thin films as the density of the domain walls is significantly higher than that of bulk materials because the lateral domain size in thin films roughly scales with the film thickness, known as Kittel's law. On the one hand, it is necessary to understand the domain formation mechanism, which is largely determined by boundary conditions such as lattice strain and electrostatics. On the other hand, the intentional manipulation of domain formation

via electric field poling, strain engineering, and/or chemical doping [4–7] provides a powerful tool to significantly improve the piezoelectric properties of thin films [8,9].

However, it is challenging to accurately predict and manipulate the as-grown domain structure and the domain switching processes in ferroelectric thin films due to the presence of mechanical and electrical boundary conditions [10,11]. Several factors contribute to this complexity, including strain gradients [12,13], interfacial effects [14,15], ion doping [16], film deposition temperature [17], and surface charges [18]. For instance, Zhao *et al.* reported a highly ordered out-of-plane polarization (self-polarization) induced by the free charges at the Pt electrode, cation vacancies at the oxide/Pt interface, and defects in  $Bi_{0.5}Na_{0.5}TiO_3$  polycrystalline films [19]. Lichtensteiger *et al.* demonstrated that the built-in electric field in  $PbTiO_3$  films is linked to the bottom electrodes and the thickness of the dielectric layer [20]. Kalinin *et al.* reported that the electrochemical reactions induced by oxygen vacancies, protons, and hydroxyls play a vital role in the domain evolution under an electric field [21].

Environmentally friendly lead-free  $K_xNa_{1-x}NbO_3$  thin films have attracted significant interest due to their excellent piezoelectric and electromechanical coupling coefficients,

\*gangniu@xjtu.edu.cn

†jutta.schwarzkopf@ikz-berlin.de

which can be tuned by strain engineering [22–24] and thus are of great potential for various functional devices. In previous work, the influence of both compressive and tensile strain on the domain structure in ferroelectric  $K_xNa_{1-x}NbO_3$  thin films has been investigated [25–28]. By employing the laser illumination on  $K_{0.70}Na_{0.30}NbO_3/TbScO_3$  samples and combining with time- and space-resolved scanning imaging x-ray-diffraction (XRD) measurement, Gaal *et al.* reported local domain formation dynamics at high spatial and temporal resolution [29]. However, the study of domain switching properties under an external electric field has been limited due to the absence of conducting bottom electrodes. Therefore, for device application reasons, it is of great significance to gain an in-depth understanding of the domain structure and its manipulation by an electric field in  $K_xNa_{1-x}NbO_3$  thin films.

In an attempt to gain a thorough understanding of the domain switching behavior in ferroelectric films, compressively strained  $K_{0.5}Na_{0.5}NbO_3$  thin films were grown on  $SrRuO_3/DyScO_3$  (110) substrates by liquid-delivery spin metal-organic vapor-phase epitaxy (MOVPE), where the  $SrRuO_3$  serves as a bottom electrode. By utilizing a combination of piezoresponse force microscopy (PFM) and high-resolution x-ray-diffraction (HRXRD) approaches, pseudocubic (pc) ferroelectric  $K_{0.5}Na_{0.5}NbO_3$  films featuring a  $90^\circ$  striped  $M_C$  domain structure with four different variants were investigated. Domain switching evolution under different bias voltages was examined using PFM, suggesting that the domain switching is only stable under positive bias due to the collective contributions of the interface effect and the strain gradient.

## II. EXPERIMENT

A 28-nm-thick, electrically conductive  $SrRuO_3$  layer was grown by pulsed laser deposition (PLD) on a  $0.1^\circ$  off-oriented  $DyScO_3$  (110) substrate, which serves as the bottom electrode for the electrical poling experiments. The PLD process was performed with a KrF excimer laser ( $\lambda = 248$  nm) with a laser frequency and fluence of 5 Hz and  $1.1$  J/cm<sup>2</sup>, respectively, at a substrate temperature of  $750^\circ$  C within an oxygen partial pressure of 15 Pa. Epitaxial  $K_{0.5}Na_{0.5}NbO_3$  films were grown on  $SrRuO_3/DyScO_3$  substrates by liquid-delivery spin MOVPE, which was performed at a substrate temperature of  $720^\circ$  C and a gas pressure of  $2.5 \times 10^3$  Pa in an Ar-O<sub>2</sub> atmosphere with an Ar/O<sub>2</sub> flux ratio of 5. K(tmhd), Na(tmhd) (thd = 2, 2, 6, 6-tetramethyl-3, 5-heptanedione), and Nb(EtO)<sub>5</sub> [(EtO)<sub>5</sub> = pentaethoxide] dissolved in dry toluene were used as the metal-organic source materials. Further details of the growth process are described in Ref. [30].

At room temperature,  $DyScO_3$  exhibits an orthorhombic symmetry ( $a = 5.442$  Å,  $b = 5.719$  Å,  $c = 7.904$  Å [31]), and it displays a nearly quadratic (110) surface unit cell with in-plane lattice parameters of  $2 \times 3.947$  and  $2 \times 3.952$  Å along the  $[1\bar{1}0]_{DSO}$  and  $[001]_{DSO}$  directions, respectively [32].  $K_{0.5}Na_{0.5}NbO_3$  also has an orthorhombic symmetry at room temperature. However, for more convenience, we use the pseudocubic (pc) notation to describe the dimensions of the  $K_{0.5}Na_{0.5}NbO_3$  unit cell by  $a_{pc} = 3.940$  Å and  $b_{pc} = c_{pc} = 4.000$  Å with an angle of  $\alpha = 89.66^\circ$  between the  $b_{pc}$  and  $c_{pc}$

axes [33–36]. As a result of the  $SrRuO_3$  and  $K_{0.5}Na_{0.5}NbO_3$  films being coherently grown on  $DyScO_3$  as shown in Fig. S1(a) (see the Supplemental Material [37]), the requirement of elastic strain energy minimization suggests a  $c_{pc}$  out-of-plane orientation of  $K_{0.5}Na_{0.5}NbO_3$  [38]. The  $K_{0.5}Na_{0.5}NbO_3$  film experiences strong compressive lattice strain along the  $b_{pc}$  axis of  $-1.21\%$  and is nearly unstrained along the  $a_{pc}$  axis ( $+0.18\%$ ), resulting in a quasiuniaxial strain state of the film unit cell.

The surface morphology was examined using atomic force microscopy (AFM, MFP3D, Asylum), which was also used for PFM measurements equipped with a dual ac resonance tracking (DART) mode in order to image the in-plane and out-of-plane polarization state in the ferroelectric domains of the  $K_{0.5}Na_{0.5}NbO_3$  films. A diamond-coated cantilever (AD-2.8-AS, Adama) was used for measurement of the domain pattern. The domain dynamic switching properties of  $K_{0.5}Na_{0.5}NbO_3$  films were explored by the lithography-PFM (litho-PFM) mode [39]. Specifically, the bias range was set from  $-4$  to  $5$  V, the setpoint was chosen to be  $1.3$  V, while the scan frequency was set to be  $0.3$  Hz. To analyze the configuration of the periodically arranged domains, a fast Fourier transformation (FFT) was performed on the measured PFM images.

To analyze the film thickness and strain state of the  $K_{0.5}Na_{0.5}NbO_3$  thin films, high-resolution x-ray diffraction (HRXRD) was carried out using a 9 kW SmartLab system (Rigaku) with a Cu  $K\alpha_1$  radiation ( $\lambda = 1.54056$  Å). Fast two-dimensional x-ray reciprocal space maps (RSMs) were recorded using a two-dimensional area detector (HyPix-3000). To determine lattice strains, film orientation, and thickness,  $2\theta$ - $\omega$  scans were performed. Cross-sectional specimens for microstructure investigation by transmission electron microscopy (TEM) were prepared using a focused ion beam system (Helios 5 CX DualBeam, FEI). The microstructure was characterized by scanning transmission electron microscopy (STEM) using FEI Tian G2 80–300 under a 300 kV acceleration voltage equipped with a Cs corrector. High-angle annular dark-field (HAADF) images and corresponding energy-dispersive spectrometer (EDS) maps were carried out to analyze elemental distribution on an atomic scale.

## III. RESULTS AND DISCUSSION

Strain-sensitive x-ray  $2\theta$ - $\omega$  scans were performed to evaluate the surface orientation, the strain state of the  $K_{0.5}Na_{0.5}NbO_3$  films grown on  $SrRuO_3/DyScO_3$  (110) substrates. Prior to HRXRD measurements, reciprocal space mappings [see Figs. S1(a) and S1(b) [37]] in the vicinity of the asymmetric (444) and (620) Bragg reflections of the  $DyScO_3$  substrate were used to verify that  $K_{0.5}Na_{0.5}NbO_3$  and  $SrRuO_3$  films are coherently grown on the  $DyScO_3$  substrate. Meanwhile, the structure of  $K_{0.5}Na_{0.5}NbO_3$  can be described with the monoclinic  $M_C$  phase, as described in Ref. [30]. Figure 1 shows the experimental  $2\theta$ - $\omega$  scan in the vicinity of the symmetrical (220) Bragg reflection of the  $DyScO_3$  substrate [the measurement around the (110)  $DyScO_3$  Bragg reflection is displayed as Fig. S1(c) [37]]. The Bragg peak of  $SrRuO_3$  appears at  $46.28^\circ$ , which is slightly higher  $2\theta$  angles than the  $DyScO_3$  (220) substrate Bragg peak. The contribution of the  $K_{0.5}Na_{0.5}NbO_3$  film can be observed over a very wide angular

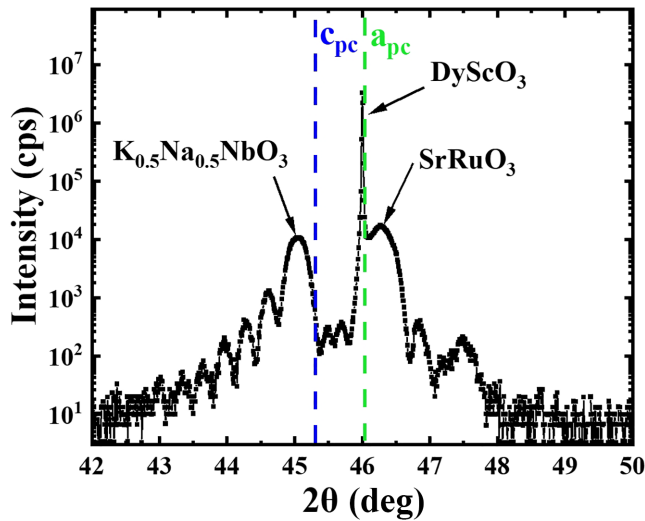


FIG. 1. High-resolution x-ray diffraction (HRXRD)  $2\theta$ - $\omega$  scan of a 32 nm  $\text{K}_{0.5}\text{Na}_{0.5}\text{NbO}_3$ /28 nm  $\text{SrRuO}_3$  sample grown on (110)  $\text{DyScO}_3$  in the vicinity of the (220)  $\text{DyScO}_3$  substrate Bragg reflection. Additionally, the positions of unstrained  $\text{K}_{0.5}\text{Na}_{0.5}\text{NbO}_3$  with  $a_{pc}$  (green) and  $c_{pc}$  (blue) orientation are marked by dotted lines.

range (i.e., Laue oscillation), and the Bragg peak appears at lower  $2\theta$  angles around  $45.04^\circ$ . Based on the simulations of the XRD data (shown, for example, in Fig. S1 [37]), we determined the position of the film peaks relative to the substrate peak position. As a result, the vertical lattice parameters for  $\text{K}_{0.5}\text{Na}_{0.5}\text{NbO}_3$  and  $\text{SrRuO}_3$  were calculated to be 4.02 and 3.92 Å, respectively. The expected  $2\theta$  positions of unstrained  $\text{K}_{0.5}\text{Na}_{0.5}\text{NbO}_3$  with  $a_{pc}$  and  $c_{pc}$  pseudocubic surface orientation (corresponding to the two different dimensions of the unit cell of unstrained  $\text{K}_{0.5}\text{Na}_{0.5}\text{NbO}_3$ ) are additionally shown

in Fig. 1 as green and blue dotted lines, respectively. This clearly verifies that the film exhibits the expected  $c_{pc}$  surface orientation. Furthermore, the thicknesses of  $\text{K}_{0.5}\text{Na}_{0.5}\text{NbO}_3$  and  $\text{SrRuO}_3$  films were also evaluated from the simulation of the HRXRD pattern to be 32 and 28 nm with an accuracy of  $\pm 1$  nm, respectively.

To investigate the ferroelectric domain structure, in-plane and out-of-plane PFM measurements were performed in a  $6\ \mu\text{m} \times 6\ \mu\text{m}$  scan area [see Figs. 2(a)–2(d)]. The orientation of the cantilever axis and the scan direction were illustrated in Fig. 2(a) as a gray arrow and a white arrow, respectively. If there is no additional explanation, this legend is suitable for all following PFM images. In the in-plane PFM images shown in Figs. 2(a) (phase image) and 2(b) (amplitude image), dark and bright areas can clearly be observed, whereas the out-of-plane PFM images shown in Figs. 2(c) (phase) and 2(d) (amplitude) exhibit a much lower contrast. This is attributed to the lower sensitivity of the vertical measurements compared to in-plane measurements [40]. In addition to the pure electromechanical contribution, the vertical signal can be influenced by local electrostatic forces (e.g., caused by surface charges), nonlocal electrostatic forces (e.g., buckling effect due to in-plane polarization), and surface morphology of the film, which influence both the amplitude and the phase signal [21]. Since the aim of this paper was not to quantify piezoelectric properties, but rather to make domain switching visible, we have rescaled the phase images in which domains with upward (downward) oriented out-of-plane polarization are clearly characterized by yellow (violet). We have omitted absolute values for the  $z$ -scale in the phase images. To illustrate this, we have used the corresponding arrow directions in the phase diagrams to indicate the polarization directions.

The in-plane PFM phase and amplitude image with higher spatial resolution shown in Figs. 2(e) and 2(f) (scan range

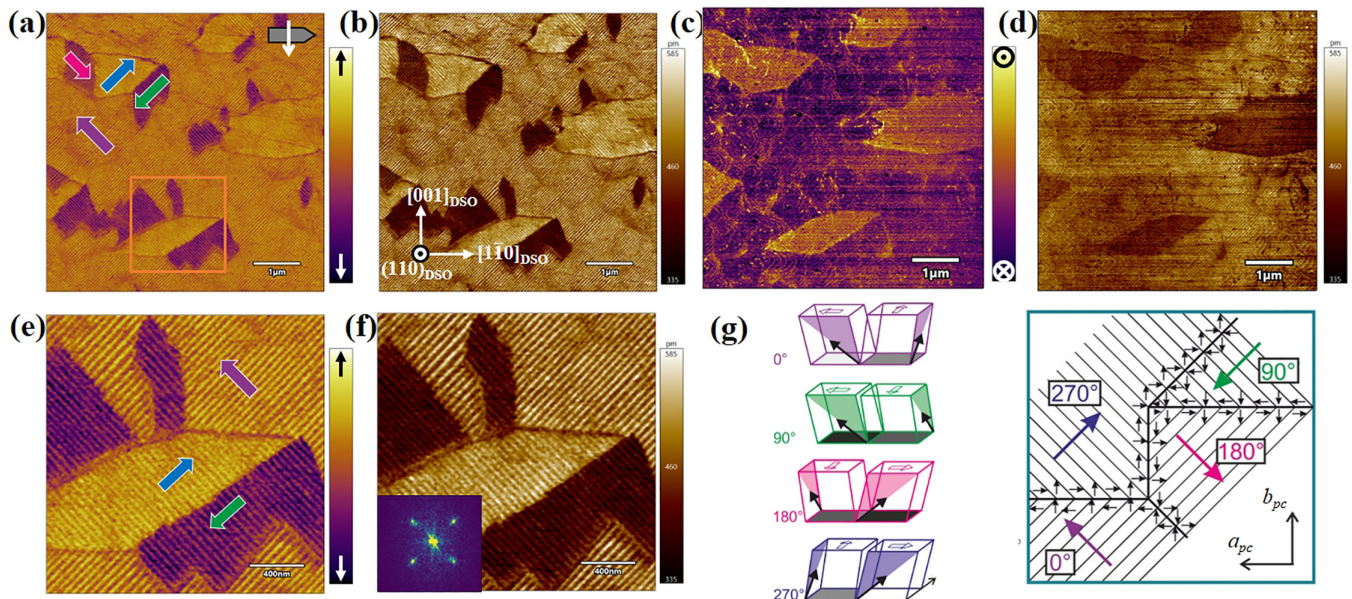


FIG. 2. PFM measurements (scan range  $6\ \mu\text{m} \times 6\ \mu\text{m}$ ) of a 32 nm  $\text{K}_{0.5}\text{Na}_{0.5}\text{NbO}_3$  film on  $\text{DyScO}_3$  (110) substrate with a 28 nm  $\text{SrRuO}_3$  bottom electrode layer: in-plane PFM (a) phase and (b) amplitude images; out-of-plane PFM (c) phase and (d) amplitude images. In-plane PFM (e) phase and (f) amplitude image extracted from the orange square in (a) with higher magnification. The inset in (f) shows the corresponding FFT pattern. (g) Schematic presentation of the four different types of superdomains in  $\text{K}_{0.5}\text{Na}_{0.5}\text{NbO}_3$  film (adapted from Ref. [30]).

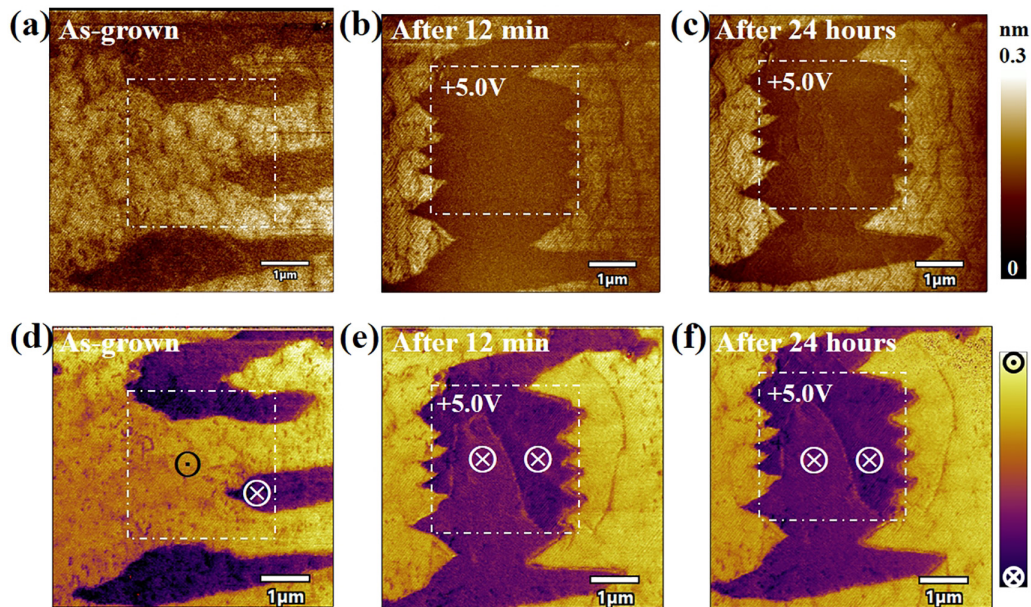


FIG. 3. Out-of-plane PFM amplitude and phase images (scan range  $6\ \mu\text{m} \times 6\ \mu\text{m}$ ): (a) and (d) as-grown domain state, (b) and (e) domain state directly after lithography step with a dc bias of +5 V, (c) and (f) domain state of 24 h after poling. These white dotted squares refer to the region where the bias voltage was applied. White (black) circles indicate the direction of the out-of-polarization component: a cross (dot) means polarization vector is downward (upward) directed.

$2\ \mu\text{m} \times 2\ \mu\text{m}$ ) reveals the occurrence of periodically arranged stripe domains along the diagonal  $[\bar{1}\bar{1}1]_{\text{DSO}}$  or  $[\bar{1}\bar{1}1]_{\text{DSO}}$  in-plane directions of the  $\text{DyScO}_3$  orthorhombic substrate, typically observed for  $M_C$  domains in  $\text{K}_x\text{Na}_{1-x}\text{NbO}_3$  films under highly anisotropic compressive strain conditions [26,30]. From the PFM images, the horizontal domain width can be extracted to be 25 nm. The FFT result of the in-plane PFM amplitude image reveals a very periodic stripe domain arrangement in both directions, based on which we evaluated an average domain width of 25 nm. This is in good agreement with the domain width of 24 nm calculated from the distance of the satellite peaks in the RSMs depicted in Fig. S1(a) [37]. According to former results [30], the in-plane polarization component of the superdomains was determined by the PFM and nanofocus XRD measurements. The stripe domain pattern consists of  $90^\circ$  domains, which can be composed of four possible combinations [see the schematic illustration on the left part of Fig. 2(g)], resulting in four different types of superdomains. The net in-plane polarization of the superdomains (sum of the in-plane polarization vectors of two adjacent  $90^\circ$  stripe domains) can be directed along the  $\pm[\bar{1}\bar{1}1]_{\text{DSO}}$  or  $\pm[\bar{1}\bar{1}1]_{\text{DSO}}$  substrate in-plane directions, marked with different colors on the right side of Fig. 2(g). All four superdomain variants were observed in the in-plane PFM images [Figs. 2(a) and 2(b)], highlighted by the corresponding colored arrows used in Fig. 2(g).

After the evaluation of the domain pattern in the as-grown state, we subsequently manipulated the domain pattern by using the litho-PFM mode where a positive or negative bias voltage is applied between the AFM tip and the bottom electrode [41]. It should be emphasized that  $M_C$  domains have both an in-plane as well as an out-of-plane polarization component; see Fig. 2(g). Out-of-plane PFM amplitude and phase images of the as-grown domain morphology are

displayed in Figs. 3(a) and 3(d), respectively, in which dark and bright regions can be observed. The direction of the out-of-plane polarization is schematically illustrated by a circle with a dot (cross) for upward (downward) orientation in bright (dark) areas in the phase image [Fig. 3(d)]. Likewise, bright and dark areas were observed in the amplitude image [Fig. 3(a)]. A series of lithography experiments with increasing positive bias was performed in order to determine the threshold bias where domains were switched. It is worth noting that lateral and vertical polarization components switch at approximately the same threshold voltage of about +4.0 V, but it is more clearly visible in LPFM (see Fig. S2 [37]). To make sure that the bias is sufficient to completely switch the domain, a bias voltage of +5.0 V dc, clearly above the threshold voltage, was applied in the white dotted square region for further investigations. The out-of-plane polarization component in this area is now exclusively directed downwards, displayed by the conversion of the bright domains to dark domains in the phase image [Fig. 3(e)]. The uniform phase and amplitude signals in the poled region indicate that all initially upward domains are mostly switched to the downward direction. To study the stability of the orientation of the domains in the polarized region, the same film area was scanned again after 24 h [Figs. 3(c) and 3(f)]. No significant polarization reversal was shown, which indicates the high stability of the downward directed domains.

For the investigation of the impact of a vertical electric field on the in-plane arrangement of the  $M_C$  domains, similar to the experiments shown in Fig. 3, positive dc bias voltages were applied between the tip and the  $\text{SrRuO}_3$  bottom electrode at different surface positions. Figure 4 shows the domain arrangement in the pristine state [Figs. 4(a) and 4(d)] and after poling in the white-marked area [Figs. 4(b) and 4(e)]. Several poling experiments were performed at different

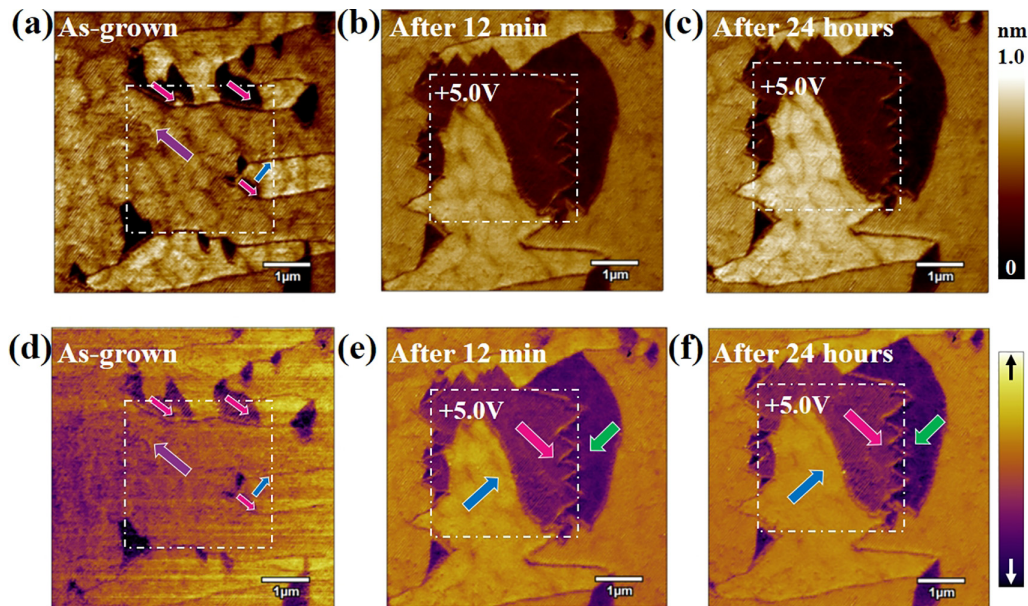


FIG. 4. In-plane PFM amplitude and phase images (scan range  $6\mu\text{m} \times 6\mu\text{m}$ ) recorded at different times: (a) and (d) as-grown domain state, (b) and (e) domain state directly after lithography step with a dc bias of +5.0 V, (c) and (f) domain state of 24 h after poling. These white dotted squares refer to the bias region.

positions with different superdomain variants in the as-grown state. The PFM data after poling clearly demonstrate that the in-plane arrangement of the stripe domains can be rotated by  $90^\circ$  [indicated by the blue and green arrows in Figs. S2(g) and S2(h)] or  $180^\circ$  [see the red arrows in Fig. S2(h) [37]] by an application of an out-of-plane voltage. This observation is tentatively explained as follows: (i) the electric field is surely not homogeneous at the tip-surface contact area (field elevation), which may cause a lateral E-field component; (ii) symmetry breaking of the rotationally invariant tip field occurs due to tip motion parallel to the surface; see Balke *et al.* [42] and Matzen *et al.* [43]. Although it was possible to change the in-plane domain arrangement, it was not feasible to establish a clear, unambiguous correlation between the original state and the switched state.

A further observation in these poling experiments is that even outside the poled region, adjacent domains are switched, which can be seen in Figs. 4(b) and 4(e) (right edge of the white square). Notably, the switched domains outside the poled region are always observed at the right side of the poled region (i.e., at the end of the lithography step), implying that this may be induced by the trailing fields due to the movement of the PFM tip. The formation of zigzag-shaped superdomain boundaries was detected, which indicates the existence of ferroelastic switching. The pronounced zigzag domain walls outside of the white dotted area are possibly caused by the minimization of the energies related to the different polarization orientations inside and outside the poled area. Please note that the domain walls are not oriented perpendicular to the surface [30], and the energy is consumed by the formation of a domain wall. To study the stability of the orientation of the domains in the polarized region under positive bias, the same film area was scanned again after 24 h [Figs. 4(c) and 4(f)]. As with the behavior observed for the out-of-plane domain, no significant polarization reversal was shown, indicating a

stable in-plane and out-of-plane domain configuration of the switched domains.

The same procedure was carried out at another sample position with a negative dc bias. The out-of-plane and in-plane as-grown domain morphologies are displayed in Figs. 5(a) and 5(d) and Figs. 6(a) and 6(d), respectively. The threshold voltage for in-plane switching was determined to be  $-3.0$  V (see Fig. S3 [37]). Subsequently, the film was poled in the marked area with  $-3.0$  V dc bias. Domain morphology was recorded directly after the poling procedure, and the corresponding out-of-plane and in-plane PFM amplitude and phase images are shown in Figs. 5(b) and 5(e) and Figs. 6(b) and 6(e), respectively. Compared to the as-grown state, the out-of-plane and in-plane amplitude of the poled region first become darker [Figs. 5(b) and 6(b)], and then they mainly turn brighter again within 1 h [Figs. 5(c) and 6(c)], respectively. For the phase signal, the out-of-plane component first becomes brighter [Fig. 5(e)] and then becomes darker again very quickly [Fig. 5(f)]. The opposite phenomenon was observed for the in-plane polarization component, while the direction of the stripes mainly stays consistent. On the contrary, at the edges of the poled region (white square), small domain switching [marked by green arrows shown in Fig. 6(e)] was observed, and the switched domains began to evolve and stabilize after 1 h [Fig. 6(f)]. These switched domains at the edge of the poled region could be attributed to the effect of the trailing field.

In addition, some brighter and darker dots are observed in the poled region in Figs. 5(b) and 5(e). When the AFM images at the same sample position were recorded (see Fig. S4 [37]), mosaiclike dots were also observed simultaneously in the poled region (white square area), as shown by the brighter dots in Fig. 5(b). Then the surface morphology is restored to its initial state within 1 h. A detailed time evaluation of the in-plane domain configuration under  $-3.0$  V bias is shown

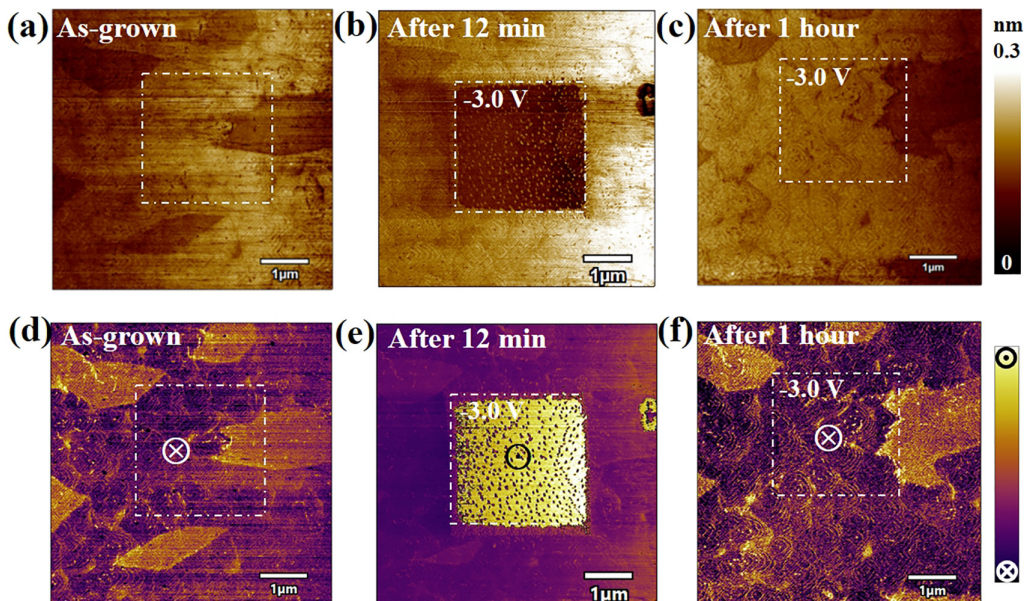


FIG. 5. Out-of-plane PFM amplitude and phase images (scan range  $6\ \mu\text{m} \times 6\ \mu\text{m}$ ): (a) and (d) as-grown domain state, (b) and (e) domain state directly after lithography step with a dc bias of  $-3.0\ \text{V}$ , (c) and (f) domain state of 1 h after poling. These white dotted squares refer to the bias region.

in Fig. S5 [37], which indicates that the domain is restored in the main part of the window within 1 h, but at the edges of the poled region the switched domain either decreases or increases depending on the size [see the domain marked by green and red arrows in Figs. 6(e) and 6(f)]. Similar to Ref. [18], it is assumed that the formation of mosaiklike dots is present in the morphology, and these “dots” in PFM images are due to the injection of surface charges. Applying a negative voltage leads to electrochemical reactions at or close

to the surface, and vacancies are created. This leads to an accumulation of surface charges, which cannot immediately be dissipated. It could be concluded that the out-of-plane domain under negative bias could not be switched, for the in-plane domain main part of it is irreversible; however, at the edges of the poled region, the domain could be switched. The time-dependent domain retention measurements were carried out (see Fig. S5 [37]), showing that the fraction of the darker area in amplitude image is reduced with time. In

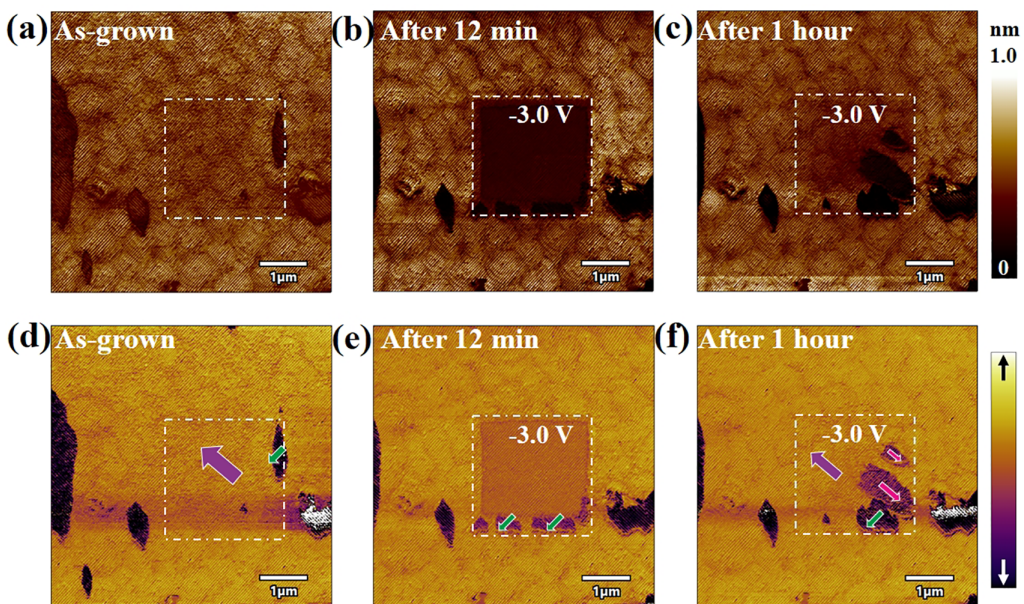


FIG. 6. In-plane PFM amplitude and phase images (scan range  $6\ \mu\text{m} \times 6\ \mu\text{m}$ ) recorded at different times: (a) and (d) as-grown domain state, (b) and (e) domain state directly after lithography step with a dc bias of  $-3.0\ \text{V}$ , (c) and (f) domain state of 1 h after poling. These white dotted squares refer to the bias region.

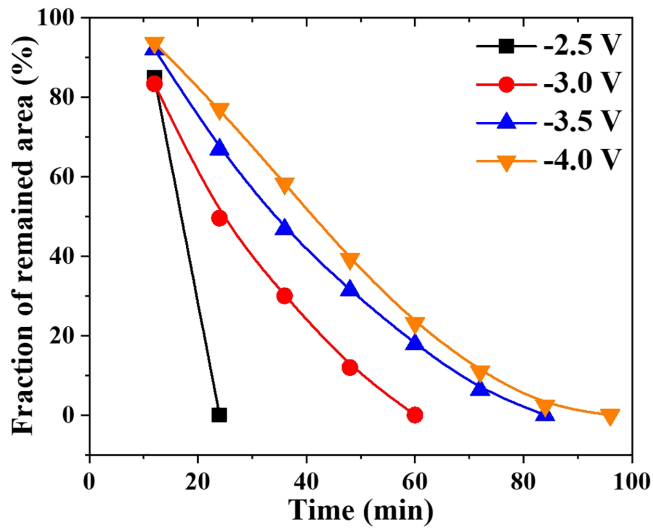


FIG. 7. Surface charge dissipation rate under different bias voltages.

contrast, the relative intensity of the amplitude signal increases with time. Similar behavior was observed under

different bias, and the results are shown in Fig. 7. Obviously, the decay depends strongly on the applied voltage. Considering that the darker areas are caused by surface charges, this result reveals the surface charge dissipation on a dielectric surface.

Since an interface plays a vital role in ferroelectric devices, an interface effect can be assumed due to the observation in Fig. S6 [37] that the out-of-plane phase and amplitude hysteresis loops are asymmetric, i.e., the switching voltage is different. Therefore, the interface of  $\text{K}_{0.5}\text{Na}_{0.5}\text{NbO}_3$  and the  $\text{SrRuO}_3$  interface have been investigated by STEM measurements. HAADF-STEM images, which are sensitive to  $z$ -contrast, are shown in Fig. 8(a) and with higher magnification in Fig. 8(b), while the  $\text{SrRuO}_3$  film shows a very cloudy contrast, which is tentatively attributed to chemical inhomogeneities and an off-stoichiometric composition, often observed in PLD films. The  $\text{K}_{0.5}\text{Na}_{0.5}\text{NbO}_3$  thin films exhibit hardly any contrast but a homogeneous intensity distribution. EDS line profiles shown in Fig. 8(c) for Ru, Nb (along the green line), and Sr, Na, K (along the blue line) indicate the relative distribution of the elements across the interface. Obviously, Nb atoms are found in the  $\text{SrRuO}_3$  films, and Sr atoms are found in the  $\text{K}_{0.5}\text{Na}_{0.5}\text{NbO}_3$  films. For a more

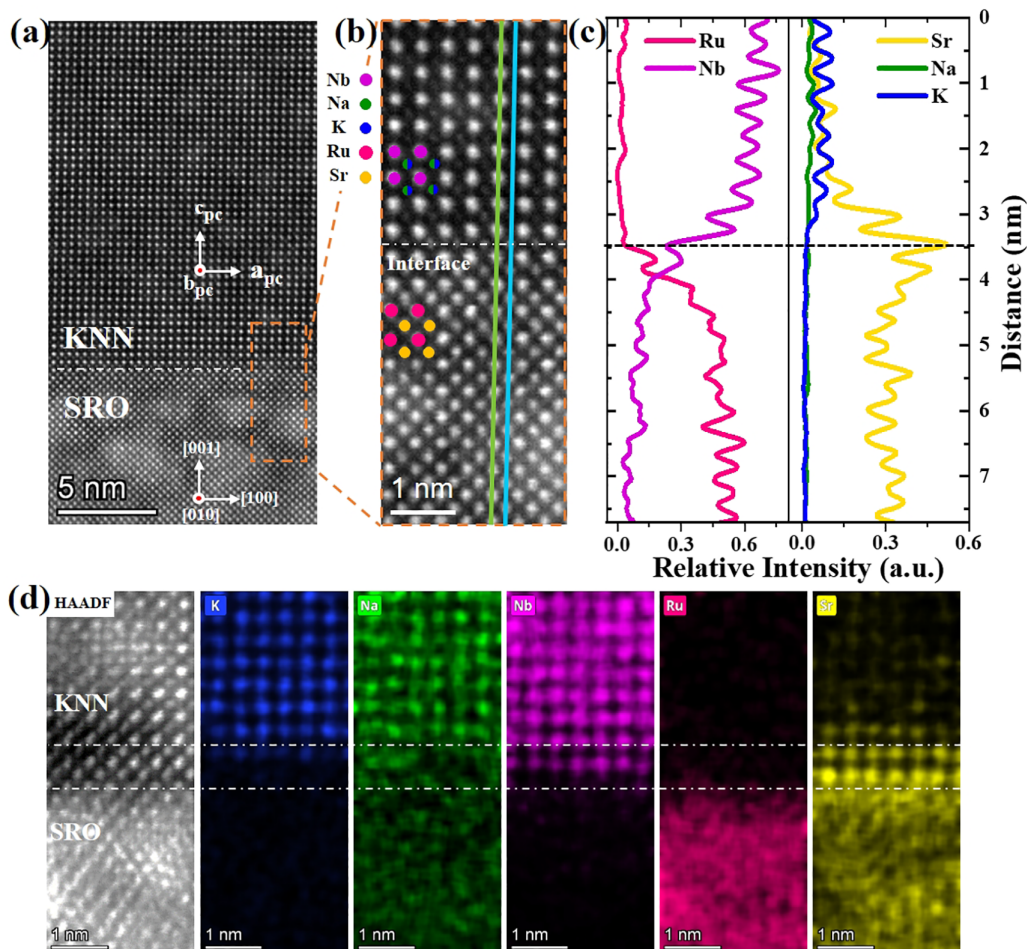


FIG. 8. (a) HAADF-STEM image of a  $\text{K}_{0.5}\text{Na}_{0.5}\text{NbO}_3/\text{SrRuO}_3$  thin film. (b) Enlarged HAADF image extracted from the orange dotted line rectangle in Fig. 8(a). (c) Line profiles of atomic columns across the interface along the vertical direction: the left image relating to the B-site (green line) and the right one relating to the A-site (cyan line) in Fig. 8(b). (d) Selected HAADF image and related composite elemental maps of K (blue), Na (green), Nb (magenta), Ru (red), and Sr (yellow), respectively.

detailed investigation, elemental mappings for K, Na, Nb, Ru, and Sr are recorded, respectively [see Fig. 8(d)]. They reveal a small intermediate layer [dedicated by the two dotted lines in Fig. 8(d)], which consists mainly of Na, Nb, and Sr elements. Furthermore, the STEM images show coherent film growth of  $\text{K}_{0.5}\text{Na}_{0.5}\text{NbO}_3$  on  $\text{SrRuO}_3$ , and no extended defects can be observed in the films. The results show, on the one hand, the high structural quality of the  $\text{K}_{0.5}\text{Na}_{0.5}\text{NbO}_3$  films. On the other hand, the intermixing layer at the interface of  $\text{K}_{0.5}\text{Na}_{0.5}\text{NbO}_3$  and  $\text{SrRuO}_3$  could be formally described as  $(\text{Na}, \text{Sr})\text{NbO}_3$ . For charge neutrality reasons, one can assume that the  $\text{Nb}^{5+}$  ions have to be reduced to  $\text{Nb}^{4+}$  provided by the existence of free electrons in the metallic  $\text{SrRuO}_3$  thin film. We assume that the asymmetric behavior of the hysteresis loops in Fig. S6 [37] is tentatively caused by the different work functions of the bottom ( $\text{SrRuO}_3$ ) and the top (diamond) electrodes. Such asymmetric phenomena of the domain configuration under a positive and a negative electric field may be attributable to the electrochemical reactions at the surface of  $\text{K}_{0.5}\text{Na}_{0.5}\text{NbO}_3$  films. This finding regarding such unexpected phenomena should also be given attention, as it may help to achieve various functional devices.

#### IV. CONCLUSIONS

In conclusion, epitaxially strained ferroelectric  $\text{K}_{0.5}\text{Na}_{0.5}\text{NbO}_3$  films were grown on  $\text{SrRuO}_3/\text{DyScO}_3$  (110) substrates by MOVPE and they experience strong anisotropic in-plane compressive strain, which leads to the formation of periodically ordered  $90^\circ M_C$  stripe domains. Domain switching behavior was investigated via litho-PFM. The out-of-plane and in-plane polarization can be reversed

under a positive electric field. Furthermore, the retention of the switched domain is examined, suggesting that with a positive electric field, both the switched out-of-plane and in-plane domains could stay stable for at least 24 h without any noticeable degeneration. However, under a negative electric field, the out-of-plane domain could not be switched, accompanied by small surface morphology changes. This behavior may be attributable to the injection of vacancies in the film surface under a negative electric field. As for the in-plane domain, the main part of it is irreversible; however, at the edges of the poled region, the domain could be switched, which may be induced by either an inhomogeneous electric field below the PFM tip, or trailing fields caused by the movement of the PFM tip across the surface. Both time-dependent PFM measurements and surface morphology reveal that surface charges will dissipate within 1 h.

#### ACKNOWLEDGMENTS

We gratefully acknowledge Natural Science Foundation of China (Grant No. M-0441), Fundamental Research Funds for the Central Universities (XZD012020059), European Regional Development Fund (ERDF) (Project No. 1.8/15), and DFG [Project ‘‘Polarization Switching Kinetics in Ferroelectric/Dielectric Bi-Layer Structures – FeDiBiS’’ (SCHM 1515/3–1)] for funding this project. The  $\text{DyScO}_3$  substrates have been grown at the Leibniz-Institut für Kristallzüchtung (IKZ) in the group of Steffen Ganschow. The authors would like to thank Jeremy Maltitz for helping with the growth of  $\text{SrRuO}_3$  films, and Marília de Oliveira Guimarães for fruitful discussions.

- 
- [1] F. Xu, S. Trolhier-McKinstry, W. Ren, B. Xu, Z.-L. Xie, and K. J. Hemker, Domain wall motion and its contribution to the dielectric and piezoelectric properties of lead zirconate titanate films, *J. Appl. Phys.* **89**, 1336 (2001).
  - [2] A. K. Tagantsev, L. E. Cross, and J. Fousek, *Domains in Ferroic Crystals and Thin Films*, edited by A. K. Tagantsev *et al.* (Springer, New York, 2010), pp. 121–206.
  - [3] J. F. Scott, Applications of modern ferroelectrics, *Science* **315**, 954 (2007).
  - [4] L. W. Martin and A. M. Rappe, Thin-film ferroelectric materials and their applications, *Nat. Rev. Mater.* **2**, 16087 (2017).
  - [5] E. Langenberg, H. Paik, E. H. Smith, H. P. Nair, I. Hanke, S. Ganschow, G. Catalan, N. Domingo, and D. G. Schlom, Strain-engineered ferroelastic structures in  $\text{PbTiO}_3$  films and their control by electric fields, *ACS Appl. Mater. Interfaces* **12**, 20691 (2020).
  - [6] C.-H. Yang, D. Kan, I. Takeuchi, V. Nagarajan, and J. Seidel, Doping  $\text{BiFeO}_3$ : Approaches and enhanced functionality, *Phys. Chem. Chem. Phys.* **14**, 15953 (2012).
  - [7] K. Wang and J.-F. Li, Domain engineering of lead-free Li-modified  $(\text{K}, \text{Na})\text{NbO}_3$  polycrystals with highly enhanced piezoelectricity, *Adv. Funct. Mater.* **20**, 1924 (2010).
  - [8] S. Wada, K. Yako, K. Yokoo, H. Kakemoto, and T. Tsurumi, Domain wall engineering in barium titanate single crystals for enhanced piezoelectric properties, *Ferroelectrics* **334**, 17 (2006).
  - [9] B. Wang, F. Li, and L.-Q. Chen, Inverse domain-size dependence of piezoelectricity in ferroelectric crystals, *Adv. Mater.* **33**, 2105071 (2021).
  - [10] K. J. Choi, M. Biegalski, Y. L. Li, A. Sharan, J. Schubert, R. Uecker, P. Reiche, Y. B. Chen, X. Q. Pan, V. Gopalan, L. Q. Chen, D. G. Schlom, and C. B. Eom, Enhancement of ferroelectricity in strained  $\text{BaTiO}_3$  thin films, *Science* **306**, 1005 (2004).
  - [11] C. Ederer and N. A. Spaldin, Effect of epitaxial strain on the spontaneous polarization of thin film ferroelectrics, *Phys. Rev. Lett.* **95**, 257601 (2005).
  - [12] N. A. Pertsev, A. G. Zembilgotov, and A. K. Tagantsev, Effect of mechanical boundary conditions on phase diagrams of epitaxial ferroelectric thin films, *Phys. Rev. Lett.* **80**, 1988 (1998).
  - [13] M. P. Cruz, Y. H. Chu, J. X. Zhang, P. L. Yang, F. Zavaliche, Q. He, P. Shafer, L. Q. Chen, and R. Ramesh, Strain control of domain-wall stability in epitaxial  $\text{BiFeO}_3$  (110) films, *Phys. Rev. Lett.* **99**, 217601 (2007).
  - [14] J. Chen, H. Lu, H.-J. Liu, Y.-H. Chu, S. Dunn, K. Ostrikov, A. Gruverman, and N. Valanoor, Interface control of surface photochemical reactivity in ultrathin epitaxial ferroelectric films, *Appl. Phys. Lett.* **102**, 182904 (2013).

- [15] M. F. Chisholm, W. Luo, M. P. Oxley, S. T. Pantelides, and H. N. Lee, Atomic-scale compensation phenomena at polar interfaces, *Phys. Rev. Lett.* **105**, 197602 (2010).
- [16] C. F. Chirila, V. Stancu, G. A. Boni, I. Pasuk, L. Trupina, L. D. Filip, C. Radu, I. Pintilie, and L. Pintilie, Controlling polarization direction in epitaxial  $\text{Pb}(\text{Zr}_{0.2}\text{Ti}_{0.8})\text{O}_3$  films through Nb (n-type) and Fe (p-type) doping, *Sci. Rep.* **12**, 755 (2022).
- [17] L. Li, J. R. Jokisaari, Y. Zhang, X. Cheng, X. Yan, C. Heikes, Q. Lin, C. Gadre, D. G. Schlom, L.-Q. Chen, and X. Pan, Control of domain structures in multiferroic thin films through defect engineering, *Adv. Mater.* **30**, 1802737 (2018).
- [18] S. V. Kalinin, S. Jesse, A. Tselev, A. P. Baddorf, and N. Balke, The role of electrochemical phenomena in scanning probe microscopy of ferroelectric thin films, *ACS Nano* **5**, 5683 (2011).
- [19] J. Zhao, W. Ren, G. Niu, N. Zhang, G. Dong, L. Wang, M. Liu, P. Shi, and Z.-G. Ye, Recoverable self-polarization in lead-free bismuth sodium titanate piezoelectric thin films, *ACS Appl. Mater. Interfaces* **9**, 28716 (2017).
- [20] C. Lichtensteiger, C. Weymann, S. Fernandez-Pena, P. Paruch, and J.-M. Triscone, Built-in voltage in thin ferroelectric  $\text{PbTiO}_3$  films: the effect of electrostatic boundary conditions, *New J. Phys.* **18**, 043030 (2016).
- [21] S. V. Kalinin, Nanoscale electric phenomena at oxide surfaces and interfaces by scanning probe microscopy, [arXiv:cond-mat/0209599](https://arxiv.org/abs/cond-mat/0209599) [cond-mat.mtrl-sci].
- [22] H. Liu, H. Wu, K. P. Ong, T. Yang, P. Yang, P. K. Das, X. Chi, Y. Zhang, C. Diao, K. A. Wong, W. E. P. Chew, Y. F. Chen, K. I. Tan, C. A. Rusydi, M. B. H. Breese, D. J. Singh, L.-Q. Chen, S. J. Pennycook, and K. Yao, Giant piezoelectricity in oxide thin films with nanopillar structure, *Science* **369**, 292 (2020).
- [23] C. Hu, X. Meng, M.-H. Zhang, H. Tian, J. E. Daniels, P. Tan, F. Huang, L. Li, K. Wang, J.-F. Li, Q. Lu, W. Cao, and Z. Zhou, Ultra-large electric field-induced strain in potassium sodium niobate crystals, *Sci. Adv.* **6**, eaay5979 (2020).
- [24] M. Schmidbauer, D. Braun, T. Markurt, M. Hanke, and J. Schwarzkopf, Strain engineering of monoclinic domains in  $\text{K}_x\text{Na}_{1-x}\text{NbO}_3$  epitaxial layers: a pathway to enhanced piezoelectric properties, *Nanotechnology* **28**, 24LT02 (2017).
- [25] L. Bogula, L. von Helden, C. Richter, M. Hanke, J. Schwarzkopf, and M. Schmidbauer, Ferroelectric phase transitions in multi-domain  $\text{K}_{0.9}\text{Na}_{0.1}\text{NbO}_3$  epitaxial thin films, *Nano Futures* **4**, 035005 (2020).
- [26] Y. Wang, S. Bin Anooz, G. Niu, M. Schmidbauer, L. Wang, W. Ren, and J. Schwarzkopf, Thickness effect on ferroelectric domain formation in compressively strained  $\text{K}_{0.65}\text{Na}_{0.35}\text{NbO}_3$  epitaxial films, *Phys. Rev. Mater.* **6**, 084413 (2022).
- [27] M.-J. Zhou, B. Wang, A. Ladera, L. Bogula, H.-X. Liu, L.-Q. Chen, and C.-W. Nan, Phase diagrams, superdomains, and superdomain walls in  $\text{K}_x\text{Na}_{1-x}\text{NbO}_3$  epitaxial thin films, *Acta Mater.* **215**, 117038 (2021).
- [28] D. Braun, M. Schmidbauer, M. Hanke, A. Kwasniewski, and J. Schwarzkopf, Tunable ferroelectric domain wall alignment in strained monoclinic  $\text{K}_x\text{Na}_{1-x}\text{NbO}_3$  epitaxial films, *Appl. Phys. Lett.* **110**, 232903 (2017).
- [29] P. Gaal, D. Schmidt, M. Khosla, C. Richter, P. Boesecke, D. Novikov, M. Schmidbauer, and J. Schwarzkopf, Self-stabilization of the equilibrium state in ferroelectric thin films, *Appl. Surf. Sci.* **613**, 155891 (2023).
- [30] L. von Helden, M. Schmidbauer, S. Liang, M. Hanke, R. Wördenweber, and J. Schwarzkopf, Ferroelectric monoclinic phases in strained  $\text{K}_{0.70}\text{Na}_{0.30}\text{NbO}_3$  thin films promoting selective surface acoustic wave propagation, *Nanotechnology* **29**, 415704 (2018).
- [31] M. Schmidbauer, A. Kwasniewski, and J. Schwarzkopf, High-precision absolute lattice parameter determination of  $\text{SrTiO}_3$ ,  $\text{DyScO}_3$  and  $\text{NdGaO}_3$  single crystals, *Acta Crystallogr. Sect. B* **68**, 8 (2012).
- [32] R. Uecker, B. Velickov, D. Klimm, R. Bertram, M. Bernhagen, M. Rabe, M. Albrecht, R. Fornari, and D. G. Schlom, Properties of rare-earth scandate single crystals (Re = Nd–Dy), *J. Cryst. Growth* **310**, 2649 (2008).
- [33] A. G. Kalinichev, J. D. Bass, and C. S. Zha, Elastic properties of orthorhombic  $\text{KNbO}_3$  single crystals by Brillouin scattering, *J. Appl. Phys.* **74**, 6603 (1993).
- [34] A. R. Denton and N. W. Ashcroft, Vegard's law, *Phys. Rev. A* **43**, 3161 (1991).
- [35] L. Wu, J. L. Zhang, C. L. Wang, and J. C. Li, Influence of compositional ratio K/Na on physical properties in  $(\text{K}_x\text{Na}_{1-x})\text{NbO}_3$  ceramics, *J. Appl. Phys.* **103**, 084116 (2008).
- [36] A. Vailionis, H. Boschker, W. Siemons, E. P. Houwman, D.H. A. Blank, G. Rijnders, and G. Koster, Misfit strain accommodation in epitaxial ABO<sub>3</sub> perovskites: Lattice rotations and lattice modulations, *Phys. Rev. B* **83**, 064101 (2011).
- [37] See Supplemental Material at <http://link.aps.org/supplemental/10.1103/PhysRevMaterials.8.054409> for the detailed XRD results, domain evolution under various applied voltage, and local phase and amplitude hysteresis loops of the  $\text{K}_{0.5}\text{Na}_{0.5}\text{NbO}_3/\text{SrRuO}_3$  films grown on (110)  $\text{DyScO}_3$  substrate.
- [38] J. Schwarzkopf, D. Braun, M. Hanke, R. Uecker, and M. Schmidbauer, Strain engineering of ferroelectric domains in  $\text{K}_x\text{Na}_{1-x}\text{NbO}_3$  epitaxial layers, *Front. Mater.* **4**, 26 (2017).
- [39] X. Qiao, W. Geng, D. Zheng, J. Ren, Y. Sun, Y. Yang, K. Bi, and X. Chou, Domain modulation in  $\text{LiNbO}_3$  films using litho piezoresponse force microscopy, *Nanotechnology* **32**, 145713 (2021).
- [40] S. V. Kalinin, B. J. Rodriguez, S. Jesse, J. Shin, A. P. Baddorf, P. Gupta, H. Jain, D. B. Williams, and A. Gruverman, Vector piezoresponse force microscopy, *Microsc. Microanal.* **12**, 206 (2006).
- [41] C. Zhao, B. Wu, K. Wang, J.-F. Li, D. Xiao, J. Zhu, and J. Wu, Practical high strain with superior temperature stability in lead-free piezoceramics through domain engineering, *J. Mater. Chem. A* **6**, 23736 (2018).
- [42] N. Balke, S. Choudhury, S. Jesse, M. Huijben, Y. H. Chu, A. P. Baddorf, L. Q. Chen, R. Ramesh, and S. V. Kalinin, Deterministic control of ferroelastic switching in multiferroic materials, *Nat. Nanotechnol.* **4**, 868 (2009).
- [43] S. Matzen, O. Nesterov, G. Rispen, J. A. Heuver, M. Biegalski, H. M. Christen, and B. Noheda, Super switching and control of in-plane ferroelectric nanodomains in strained thin films, *Nat. Commun.* **5**, 4415 (2014).